ADVANCING EARTH AND SPACE SCIENCES

Geophysical Research Letters

RESEARCH LETTER
10.1029/2024GL113231

Key Points:

- Juno's first-year radio occultation data were analyzed providing insights into Jupiter's atmosphere
- A ray-tracing-based algorithm designed for two-way radio occultations was employed to retrieve detailed atmospheric profiles
- Uncertainty quantification of pressure and temperature measurements was carried out

Correspondence to:

A. Caruso,
andrea.caruso15@unibo.it

Citation:

Caruso, A., Gomez Casajus, L., Smirnova, M., Buccino, D., Galanti, E., Hubbard, W. B., et al. (2025). Probing Jupiter's atmosphere through Juno Radio occultations: Methodology and initial observations. *Geophysical Research Letters*, *52*, e2024GL113231. https://doi.org/10.1029/2024GL113231

Received 25 OCT 2024
Accepted 12 MAY 2025

Probing Jupiter's Atmosphere Through Juno Radio Occultations: Methodology and Initial Observations

Andrea Caruso[1,2], Luis Gomez Casajus[1,2], Maria Smirnova[3], Dustin Buccino[4], Eli Galanti[3], William B. Hubbard[5], Andrea Togni[1], Edoardo Gramigna[1,2], Marzia Parisi[4], Ryan S. Park[4], Marco Zannoni[1,2], Paul G. Steffes[6], Steven M. Levin[4], Scott J. Bolton[7], Paolo Tortora[1,2], and Yohai Kaspi[3]

[1]Department of Industrial Engineering, University of Bologna, Forlì, Italy, [2]Centro Interdipartimentale di Ricerca Industriale Aerospaziale, University of Bologna, Forlì, Italy, [3]Department of Earth and Planetary Sciences, Weizmann Institute of Science, Rehovot, Israel, [4]Jet Propulsion Laboratory, California Institute of Technology, Pasadena, CA, USA, [5]Lunar and Planetary Laboratory, University of Arizona, Tucson, AZ, USA, [6]School of Electrical and Computer Engineering, Georgia Institute of Technology, Atlanta, GA, USA, [7]Southwest Research Institute, San Antonio, TX, USA

Abstract This paper presents an analysis of Juno's first radio occultation experiments. Relying on two-way radio links in the X- and Ka-bands, we processed data from NASA's Deep Space Network antennas through a ray-tracing inversion algorithm. By effectively isolating dispersive effects, we obtained measurements of the neutral atmosphere's characteristics. This enabled the derivation of pressure and temperature profiles from the recorded frequencies. These results complement prior data from Voyager occultations and CIRS observations, providing valuable contributions to our understanding of Jupiter's atmospheric dynamics.

Plain Language Summary This manuscript explains how Juno's radio signals were used to study Jupiter's atmosphere in a set of occultation experiments. By analyzing how the frequency changed as the signals passed through Jupiter's atmosphere, we were able to measure atmospheric properties, such as pressure and temperature. These findings add to the knowledge we gained from previous missions, such as Voyager, and help us understand how Jupiter's atmosphere behaves.

1. Introduction

The Juno mission, which arrived at the Jupiter system on 5 July 2016, is designed to study Jupiter in unprecedented detail. Its primary goal is to better understand the planet's internal structure, atmosphere, and magnetosphere (Bolton et al., 2017). The Juno extended mission, approved in 2021, builds upon the success of the original Juno mission, allowing the spacecraft to continue exploring Jupiter and its surrounding environment until at least 2025.

A key component of Juno is the Radio Science Experiment (Asmar et al., 2017), which uses radio signals to precisely measure changes in Jupiter's gravitational field (Durante et al., 2020). As part of the extended mission, starting from Perijove (PJ) 53 on 31 July 2023, the spacecraft began using the radio science subsystem to also conduct radio occultation experiments to investigate Jupiter's atmosphere (Buccino et al., 2023). Juno has already executed occultation experiments during flybys of Ganymede (Buccino et al., 2022) and Europa (Parisi et al., 2023). These experiments occur when a spacecraft passes behind a planetary body, as seen from Earth, causing its radio signals to pass through the body's atmosphere. Due to the effect of refraction, the signal's path bends, and the radio signal undergoes a phase shift. As a result, the Earth's antenna records a signal with a frequency different from what would have been observed if the signal had propagated through a vacuum. This difference, called Doppler residual frequency, can be used as an input to inversion methods to yield temperature and pressure profiles of atmospheres (Schinder et al., 2020) or measure electron density within plasma environments (Withers & Moore, 2020). To date, numerous radio occultation experiments have been successfully carried out at different planets such as Mars (Fjeldbo & Eshleman, 1968; Kliore et al., 1965), Venus (Gramigna et al., 2023; Jenkins et al., 1994; Pätzold et al., 2007), Saturn (Schinder et al., 2011a), and Pluto (Hinson et al., 2017).

Additional Jupiter radio occultations by Juno were later carried out during PJ54 (7 September 2023), PJ60 (9 April 2024), PJ61 (12 May 2024), PJ62 (13 June 2024), and PJ63 (16 July 2024) as two-way, dual-frequency

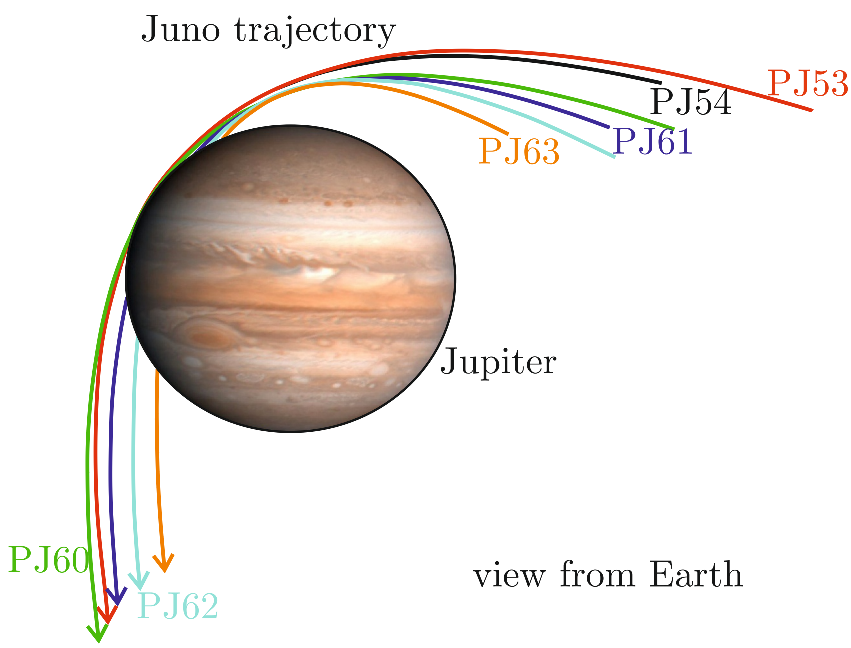

Figure 1. Schematic representation of the geometry of Juno radio occultation experiments that occurred during PJ53 to PJ63.

experiments. Juno's radio science instrumentation can operate in one of these modes during an occultation (Buccino et al., 2023):

- X/X + X/Ka: X-band downlink (8.4 GHz) and Ka-band downlink (32 GHz) phase coherent with an X-band uplink (7.1 GHz)
- X/X + Ka/Ka: X-band downlink (8.4 GHz) phase coherent with an X-band uplink (7.1 GHz) and Ka-band downlink (32 GHz) phase coherent with a Ka-band uplink (34 GHz)

The occultation geometry is depicted in Figure 1 for the occultations occurring between PJ53 and PJ63. Note that, the experiments occurred during PJ53, 54 and 60 were grazing occultations, that is, the spacecraft's radio signal passed tangentially through the atmosphere. This led to atmospheric profiles that encompass a wide span of latitudes.

The aim of this paper is to describe the methodology used to analyze the open-loop data collected during the first year of the Juno extended mission with the objective of presenting the vertical profiles of pressure and temperature within Jupiter's atmosphere. We also provide the uncertainties associated to each profile due to different effects: the observed noise in the Doppler residual frequency, the uncertainty in the wind measurements, and the uncertainty in the Juno's trajectory (Schinder et al., 2011a, 2011b). Juno's observations mark the first radio occultation measurements of Jupiter's neutral atmosphere since the earlier measurements from the Voyager missions (Lindal et al., 1981), as the Galileo High Gain Antenna failed to deploy and the radio science experiment was unable to conduct atmospheric occultations of Jupiter (Hinson et al., 1997). Therefore, these data offer a unique opportunity to study Jupiter's structure and dynamics with modern instrumentation.

2. Methodology

This section outlines the methodology used to process data from Juno's radio occultations, which use a two-way radio link. In the following, the superscript "up" will denote the uplink signal, and "dn" will refer to the downlink signal. A signal is transmitted from the ground station A to the spacecraft B during the uplink phase, with a frequency f_A sent at time t_A. The spacecraft receives this signal at time t_B^{up} with frequency f_B^{up}. The on-board electronics multiplies it by a turn-around ratio Λ, and retransmits it during the downlink phase with frequency $f_B^{\mathrm{dn}} = \Lambda f_B^{\mathrm{up}}$. This downlink signal is received by the ground station C at time t_C with frequency f_C.

The positions of the ground station, $\boldsymbol{r}_A$ and $\boldsymbol{r}_C$, differ between transmission and reception, while the spacecraft position is $\boldsymbol{r}_B$. The positions of Juno, the ground station, and other celestial bodies are provided by the Navigation

Team in the form of SPICE kernels (Acton, 1996). Additionally, the uplink transmission frequency f_A is measured by the ground station transmitter system, and the time series of the downlink frequencies f_C can be extracted from the data recorded at the ground station, as described below.

2.1. Doppler Residual Frequency

Traditional closed-loop radiometric tracking cannot be used for radio occultations because of the frequency variations induced by the occultation event, as changes in the frequency content cannot be followed by the tracking architecture without the inclusion of additional noise to the measurement. Juno occultation data are collected at NASA's Deep Space Network antennas using an open-loop technique, where a wide bandwidth around the predicted downlink frequency is recorded for later processing. The objective is to generate a time series of frequencies in spite of changes in the power or frequency of the recorded signal. To this aim, Discrete Fourier Transform (DFT)-based methods or phase-locked loops (PLL) are used. DFT-based methods analyze signals in the frequency domain (Rife & Boorstyn, 1974), whereas phase-based estimations use a numerically controlled oscillator to match the received frequency (Chang, 2015). While PLL-based estimations can generally achieve higher accuracy than DFT-based methods, their use is limited by the residual dynamics of the downlink frequency, which may cause the PLL to lose track of the signal. As a result, DFT-based methods are typically preferred, although in some cases, PLL estimation can help reduce the frequency reconstruction error, as in the case of the occultation occurred during PJ53 as will be shown later.

In a two-way radio occultation experiment, the downlink recorded frequency differs from the transmitted uplink frequency due to three key effects: relative motion between the antennas, dispersive effects, and the effect due to neutral molecules.

When the X and Ka band radio signals pass through a region of charged particles, such as Jupiter's ionosphere or the Io Plasma Torus (Moirano et al., 2021; Phipps et al., 2021), different frequencies are affected differently as they interact with the plasma, leading to frequency-dependent shifts. In particular, the dispersive contribution is proportional to f^{-2}, with f the frequency. Dalba and Withers (2019) show in the case of a dual-link X/X + X/Ka that a linear combination of the received frequencies can be used to isolate the dispersive effects along the downlink leg (referring e.g. to the X band), that is

$$\Delta f_i^{\mathrm{dn}} = \frac{f_{C,X} - (880/3360) f_{C,K}}{1 - (880/3360)^2} \tag{1}$$

where $f_{C,X}$ and $f_{C,K}$ are the recorded frequencies at X and Ka bands, respectively, and 880/3360 is the ratio of X-band to Ka-band signal frequencies transmitted by Juno. Moreover, since these radio occultations are conducted in two-way mode, and the plasma sources we aim to isolate are located near the spacecraft, the uplink contribution can be evaluated as $\Delta f_i^{\mathrm{up}} = \Delta f_i^{\mathrm{dn}} \times \Lambda^2$, and, therefore, the two-way Doppler residuals due solely to dispersive sources can be written as

$$\Delta f_i = \Delta f_i^{\mathrm{dn}} + \Delta f_i^{\mathrm{up}} = \frac{f_{C,X} - (880/3360) f_{C,K}}{1 - (880/3360)^2} \left(1 + \Lambda^2\right) \tag{2}$$

Since Juno maintains a fixed attitude during the occultations, and because the beamwidth of the Ka-band signal (0.2 deg) is narrower than that of the X-band signal (0.43 deg), the bending due to atmospheric refraction causes the Ka-band signal to experience extinction earlier. As a result, in regions where Ka-band data are missing, the calibration of the dispersive effects cannot be performed. In these cases, only the X-band data are used for the analysis. Otherwise, this effect can be directly removed from the recorded frequencies, resulting in frequencies calibrated for dispersive effects (e.g. at X band)

$$\tilde{f}_{C,X} = f_{C,X} - \Delta f_i \tag{3}$$

For the sake of conciseness, in the case of a dual-link X/X + Ka/Ka, we do not include the full methodology for isolating the dispersive effects. However, all the details can be found in (Mariotti & Tortora, 2013).

As the spacecraft and Earth-based antenna move relative to each other, the frequency of the signal is shifted. The frequency of the downlink signal received by the ground station if both uplink and downlink rays traveled in a vacuum can be computed as

$$f_{\mathrm{vac}} = \Lambda \left(\frac{f_C}{f_B}\right)^{\mathrm{dn}}_{\mathrm{vac}} \left(\frac{f_B}{f_A}\right)^{\mathrm{up}}_{\mathrm{vac}} f_A \tag{4}$$

where the terms $\left(f_B/f_A\right)^{\mathrm{up}}_{\mathrm{vac}}$ and $\left(f_C/f_B\right)^{\mathrm{dn}}_{\mathrm{vac}}$ represent the Doppler shift in a vacuum that can be computed using the following (Schinder et al., 2015)

$$\left(\frac{f_B}{f_A}\right)^{\mathrm{up}}_{\mathrm{vac}} = \frac{1 - \hat{\boldsymbol{s}}^{\mathrm{up}}_{\mathrm{vac}} \cdot \boldsymbol{v}_B/c}{1 - \hat{\boldsymbol{s}}^{\mathrm{up}}_{\mathrm{vac}} \cdot \boldsymbol{v}_A/c} \sqrt{\frac{1 - 2U(\boldsymbol{r}_A)/c^2 - v_A^2/c^2}{1 - 2U(\boldsymbol{r}_B)/c^2 - v_B^2/c^2}} \tag{5}$$

$$\left(\frac{f_C}{f_B}\right)^{\mathrm{dn}}_{\mathrm{vac}} = \frac{1 - \hat{\boldsymbol{s}}^{\mathrm{dn}}_{\mathrm{vac}} \cdot \boldsymbol{v}_C/c}{1 - \hat{\boldsymbol{s}}^{\mathrm{dn}}_{\mathrm{vac}} \cdot \boldsymbol{v}_B/c} \sqrt{\frac{1 - 2U(\boldsymbol{r}_B)/c^2 - v_B^2/c^2}{1 - 2U(\boldsymbol{r}_C)/c^2 - v_C^2/c^2}} \tag{6}$$

with v_A, v_B and v_C the norm of $\boldsymbol{v}_A$, $\boldsymbol{v}_B$ and $\boldsymbol{v}_C$ being the velocities of the Earth's antenna at time t_A, of Juno at time t_B, and Earth's antenna at time t_C, respectively. The unit vectors $\hat{\boldsymbol{s}}^{\mathrm{up}}_{\mathrm{vac}}$ and $\hat{\boldsymbol{s}}^{\mathrm{dn}}_{\mathrm{vac}}$ are the vacuum directions for the uplink and downlink rays (assuming the signal propagates along a straight line in a vacuum). Equations 5 and 6 are accurate to the order c^{-2} with c being the speed of light in a vacuum, and $U(\boldsymbol{r})$ is the gravitational potential computed at the position $\boldsymbol{r}$.

As we focus on the analysis of Jupiter's neutral atmosphere, we remove the influence of nearby plasma and Doppler effect on the received signal, to isolate the only contribution coming from the neutral molecules, that is

$$\Delta f_n = \tilde{f}_{C,X} - f_{\mathrm{vac}} \tag{7}$$

Prior to an ingress occultation or following an egress occultation, there is a period called baseline, during which the signal passes through a vacuum. Ideally, the residual frequency Δf_n during this interval should be zero. However, various factors such as interplanetary plasma, Earth's troposphere and ionosphere, and spacecraft trajectory errors typically cause deviations from zero. To address this, a linear least squares fit is applied to the baseline Doppler residuals, and the recorded frequency $\tilde{f}_{C,X}$ is corrected to remove any trends or biases, resulting in residuals with a zero mean value (Schinder et al., 2015).

2.2. Atmospheric Model

In our analysis, we assume that Jupiter's atmosphere is in hydrostatic equilibrium and barotropic, that is, surface of constant density ρ and pressure p coincide. To ensure this, the fluid angular velocity must be constant on cylinders centered on the planet's axis of rotation (Poisson & Will, 2014). Also, it can be demonstrated that surfaces of constant density and pressure coincide with surfaces of constant potential Φ, given by the sum of a gravitational and a centrifugal term (Poisson & Will, 2014), viz.

$$\Phi(r,\theta) = -\frac{\mu}{r}\left[1 - \sum_{i=2}^{N_J} J_i P_i(\sin\theta)\left(\frac{R}{r}\right)^i\right] - \int_0^{R_c} \omega^2 R_c \mathrm{d}R_c, \tag{8}$$

where $\mu = 126\,686\,534.1\ \mathrm{km^3/s^2}$ is Jupiter's gravitational parameter (Durante et al., 2020), r is the distance from the planet's barycenter, J_i is the ith zonal harmonics, P_i is the ith Legendre polynomial, θ is the planetocentric latitude, R is a reference radius, $R_c = r\cos\theta$ is the distance from the axis of rotation, and ω is the angular velocity. The latter is given by the sum of the solid-body rotation Ω and a term that depends on the zonal wind velocity V_w, that is

$$\omega = \Omega + \frac{V_w}{R_c}. \tag{9}$$

As for the solid-body rotation, $\Omega \simeq 1.7585 \times 10^{-4}$ rad/s, which corresponds to a Jupiter's rotation period of 9 h 55 m 29.771 s (Limaye, 1986). The measured wind velocities V_w are obtained using feature tracking technique (Tollefson et al., 2017; Wong et al., 2020) and are assumed attached to an equipotential surface at a given pressure level (100 mbar in this analysis) (Galanti et al., 2023; Lindal et al., 1985). Thus, the wind angular velocity is assumed constant on cylindrical surfaces.

The density of the atmospheric fluid can be expressed as (Withers, 2010)

$$\rho = \overline{m}\, n_n = \overline{m}\, \frac{N}{\mathcal{N}_v}, \tag{10}$$

where n_n is the total number density, $N = n - 1$ is the refractivity and n is the refractive index. Therefore, the surfaces of constant refraction N also coincide with the equipotential surfaces. In Equation 10, the mean molecular mass $\overline{m}$ and mean refractive volume $\mathcal{N}_v$ can be evaluated once we made some assumptions on the neutral atmosphere composition. The volume mixing ratios of gases in the atmosphere of Jupiter is 86.23% H_2, 13.56% He, 0.20437% CH_4, 0.00214% Ne, 0.00157% Ar, 0.0001863% PH_3 (Gupta et al., 2022). As a result, we can estimate a value of $\overline{m} \simeq 3.844 \times 10^{-27}$ kg and $\mathcal{N}_v \simeq 4.562 \times 10^{-33}$ km^3.

For a fluid in hydrostatic equilibrium the following equality holds

$$\mathrm{d}p = -\rho\, \mathrm{d}\Phi. \tag{11}$$

Moreover, within the assumption of ideal gas, the following equation of state can be introduced

$$p = k_B\, n_n\, T, \tag{12}$$

where T is the temperature and k_B is the Boltzmann constant. Thus, an expression for the temperature can be obtained combining Equations 11 and 12 as follows

$$T = T(\Phi_0)\, \frac{n_n(\Phi_0)}{n_n} - \frac{1}{k_B n_n} \int_{\Phi_0}^{\Phi} \rho\, \mathrm{d}\Phi, \tag{13}$$

where Φ_0 is a reference potential level at which a suitable upper boundary condition $T(\Phi_0)$ is enforced (Fjeldbo & Eshleman, 1968).

The procedure that will be described in the following subsection let us obtain a vertical profile of refractive index $n = n(\Phi)$ from the time series of received frequencies. Thus, Equation 10 can be used to compute ρ and n_n. Then, once the temperature profile has been calculated with Equation 13, the pressure is obtained from Equation 12.

2.3. Inversion Method

The methodology that is here presented for the inversion of radio occultation data is mainly based on the ray-tracing approach presented by Schinder et al. (2015). In this study we assume geometric optics holds, and, therefore, each data point in the time series corresponds to a pair of uplink/downlink rays. Moreover, we assume that the atmosphere is composed of concentric shells, and the gas properties within each shell are calculated using an iterative procedure, layer by layer. Also, each shell will correspond to a specific frequency data point. Therefore, the shorter the count time for the observables, the higher the shell number, resulting in higher resolution for the vertical profiles of atmospheric properties.

First of all, let us introduce an inertial reference frame $\mathcal{R}(O; x, y, z)$ where O is the Jupiter's barycenter and the z-axis is aligned with its axis of rotation. Recalling that surfaces of constant refractivity coincide with surfaces of constant potential, the gradient of the refractive index is parallel to the gradient of Φ. Moreover, if the thickness of each layer is much smaller than the refractivity scale height, it can be reasonably assumed that the refractive index varies linearly within each shell (Caruso et al., 2023), that is

$$n = n_k - \alpha_k (\Phi - \Phi_k) \tag{14}$$

where n_k and Φ_k are the refractive index and the potential evaluated at the upper boundary of the kth shell, and

$$\alpha_k = -\frac{\mathrm{d}n}{\mathrm{d}\Phi} \tag{15}$$

inside the kth shell is an unknown quantity to be determined. Therefore

$$\nabla n = \left[\frac{\partial n}{\partial x}, \frac{\partial n}{\partial y}, \frac{\partial n}{\partial z}\right]^{\mathrm{T}} = -\alpha_k \nabla\Phi. \tag{16}$$

We now outline the procedure to obtain the refractive index profile $n = n(\Phi)$. It is important to note that for a neutral gas, the refractive index is frequency-independent and will be the same for both the uplink and downlink rays. The first step involves defining the boundary of Jupiter's atmosphere. We select an arbitrary time instant $t_C^{(0)}$, chosen such that the signal is still outside the atmosphere. We assume the signal travels along a straight line as it propagates through a vacuum. Along the raypath (both uplink and downlink), we determine the point at which the potential is minimal. Then, we assume that all points on the surface at this potential constitute the boundary of the atmosphere.

At the subsequent time $t_C^{(1)}$, a new pair of uplink and downlink signals is considered, and the entire atmosphere is treated as a single shell. We can evaluate the (uplink and downlink) raypath as it traverses Jupiter's atmosphere using Equation 4 from Schinder et al. (2015). We assume that the direction of the uplink raypath upon reaching Juno is $\hat{\boldsymbol{s}}_B^{\mathrm{up}}$, and that the direction of the downlink raypath upon retransmission by Juno is $\hat{\boldsymbol{s}}_B^{\mathrm{dn}}$. The downlink ray is integrated by enforcing that the initial position coincides with that of Juno, $\boldsymbol{r}_B$, and the initial direction is $\hat{\boldsymbol{s}}_B^{\mathrm{dn}}$. Note that, due to numerical considerations, we integrate the uplink ray backward in time, from Juno's position $\boldsymbol{r}_B$ to the location of the ground antenna that transmitted the uplink signal, assuming the initial condition on the direction for the latter as $-\hat{\boldsymbol{s}}_B^{\mathrm{up}}$. Note that, while Juno's position is assumed to be known at each time instant, the initial directions of the ray paths, $\hat{\boldsymbol{s}}_B^{\mathrm{dn}}$ and $-\hat{\boldsymbol{s}}_B^{\mathrm{up}}$, are unknown quantities that will be determined using the numerical procedure outlined below.

The numerical integration of Equation 4 of Schinder et al. (2015) allows us to determine the position of the point where the raypath leaves Jupiter's atmosphere for both the uplink and downlink signals, denoted as $\boldsymbol{r}_E^{\mathrm{up}}$ and $\boldsymbol{r}_E^{\mathrm{dn}}$, respectively, as well as the direction at that point, $\hat{\boldsymbol{s}}_E^{\mathrm{up}}$ and $\hat{\boldsymbol{s}}_E^{\mathrm{dn}}$. Subsequently, the following conditions are imposed. First, the direction of the signal after leaving the atmosphere is required to point toward the ground antenna, that is

$$\hat{\boldsymbol{s}}_E^{\mathrm{up}} - \frac{\boldsymbol{r}_A - \boldsymbol{r}_E^{\mathrm{up}}}{\left\|\boldsymbol{r}_A - \boldsymbol{r}_E^{\mathrm{up}}\right\|} = 0 \tag{17}$$

$$\hat{\boldsymbol{s}}_E^{\mathrm{dn}} - \frac{\boldsymbol{r}_C - \boldsymbol{r}_E^{\mathrm{dn}}}{\left\|\boldsymbol{r}_C - \boldsymbol{r}_E^{\mathrm{dn}}\right\|} = 0 \tag{18}$$

Furthermore, the signal must reach the ground antenna with a frequency equal to the one actually recorded. According to Bourgoin et al. (2019), the ratio of the Doppler frequency shift when atmospheric refraction occurs to the vacuum contribution can be expressed as

$$\chi^{\mathrm{up}} = \frac{f_B^{\mathrm{up}}/f_A}{\left(f_B/f_A\right)_{\mathrm{vac}}^{\mathrm{up}}} = \frac{1 - \frac{\left(\hat{\boldsymbol{s}}_B^{\mathrm{up}} - \hat{\boldsymbol{s}}_{\mathrm{vac}}^{\mathrm{up}}\right)\cdot \boldsymbol{v}_B/c}{1 - \hat{\boldsymbol{s}}_{\mathrm{vac}}^{\mathrm{up}}\cdot \boldsymbol{v}_B/c}}{1 - \frac{\left(\hat{\boldsymbol{s}}_A - \hat{\boldsymbol{s}}_{\mathrm{vac}}^{\mathrm{up}}\right)\cdot \boldsymbol{v}_A/c}{1 - \hat{\boldsymbol{s}}_{\mathrm{vac}}^{\mathrm{up}}\cdot \boldsymbol{v}_A/c}} \tag{19}$$

$$\chi^{\mathrm{dn}} = \frac{f_C/f_B^{\mathrm{dn}}}{\left(f_C/f_B\right)_{\mathrm{vac}}^{\mathrm{dn}}} = \frac{1 - \frac{\left(\hat{\boldsymbol{s}}_C - \hat{\boldsymbol{s}}_{\mathrm{vac}}^{\mathrm{dn}}\right)\cdot \boldsymbol{v}_C/c}{1 - \hat{\boldsymbol{s}}_{\mathrm{vac}}^{\mathrm{dn}}\cdot \boldsymbol{v}_C/c}}{1 - \frac{\left(\hat{\boldsymbol{s}}_B^{\mathrm{dn}} - \hat{\boldsymbol{s}}_{\mathrm{vac}}^{\mathrm{dn}}\right)\cdot \boldsymbol{v}_B/c}{1 - \hat{\boldsymbol{s}}_{\mathrm{vac}}^{\mathrm{dn}}\cdot \boldsymbol{v}_B/c}} \tag{20}$$

where $(f_B/f_A)^{\mathrm{up}}_{\mathrm{vac}}$ and $(f_C/f_B)^{\mathrm{dn}}_{\mathrm{vac}}$ are obtained from Equations 5 and 6, whereas $\hat{\boldsymbol{s}}_A$ and $\hat{\boldsymbol{s}}_C$ are the unit direction vectors of the raypath leaving the antenna in uplink and arriving at the antenna in downlink, respectively. Therefore, the received frequency can be expressed as (Caruso et al., 2023)

$$f_C = \Lambda \chi^{\mathrm{dn}} \chi^{\mathrm{up}} \left(\frac{f_C}{f_B}\right)^{\mathrm{dn}}_{\mathrm{vac}} \left(\frac{f_B}{f_A}\right)^{\mathrm{up}}_{\mathrm{vac}} f_A \tag{21}$$

Equations 17, 18 and 21 constitute a set of equations in the unknowns $\hat{\boldsymbol{s}}^{\mathrm{up}}_B$, $\hat{\boldsymbol{s}}^{\mathrm{dn}}_B$, and α_k with $k = 1$ for this first shell. Since $\hat{\boldsymbol{s}}^{\mathrm{up}}_B$ and $\hat{\boldsymbol{s}}^{\mathrm{dn}}_B$ are unit vectors, only two of their three components will be unknowns, resulting in a system of five equations with five unknowns, which can be solved using standard numerical methods. Subsequently, the point of minimum potential along the downlink and uplink rays is evaluated, and the surface at that potential will define the outer boundary of a second shell, while the refractive index gradient within the first shell is fixed at the value of α_1.

At the subsequent time step $t_C^{(2)}$, a new pair of uplink/downlink rays is traced through the atmosphere. The new rays will first pass through the shell whose properties are already known, before reaching the deepest shell whose properties now need to be determined. To this end, the previously described procedure is applied, solving the set of Equations 17, 18 and 21 to determine the directions of the uplink and downlink rays and the refractive index gradient of the new deepest shell, α_2. This process is then iterated to obtain all the values of α_k. The refractive index can then be calculated using Equation 14 within each shell, enforcing the condition that at the boundary of the first shell, $n = 1$ (vacuum condition). Finally, pressure and temperature can be computed as described in Subsection 2.2.

3. Uncertainty Quantification

In calculating Jupiter's pressure and temperature profiles, it's crucial to assess uncertainties from various factors. Our analysis focuses on four main effects: (a) the imperfect knowledge of a boundary condition for temperature; (b) uncertainties in zonal winds measurements; (c) noise in the Doppler frequency residuals; (d) uncertainties in Juno's trajectory. Below, we outline how we evaluated these effects.

In the retrieval of the vertical profiles we first need to set a proper boundary condition on the value of temperature at a given potential level, $T(\Phi_0)$, as discussed in Subsection 2.2. In particular, in accordance with Simon-Miller et al. (2006), we assume a temperature of 160 ± 10 K at a potential level corresponding to a pressure of 1 mbar.

In this work, we also sought to assess the effect of uncertainty in the zonal wind speed values. To this end, we assumed different wind measurements attached to the equipotential surface corresponding to a pressure of 100 mbar. Specifically, we used the values reported by Tollefson et al. (2017) and Wong et al. (2020). We also considered wind profiles consistent with the gravity measurements obtained in the analysis by Galanti et al. (2023). Then, we estimated, for each pressure level, the standard deviation in the temperature measurements.

Also, we wanted to quantify the effect of the observed noise in Doppler observables. The latter is due to the sum of various contributions: thermal noise, noise introduced by Earth's atmosphere and ionosphere, and solar plasma. As an example, Figure 2 depicts the Doppler frequency residual for the occultations that occurred during PJ53 and PJ63. In particular, the upper panels report the Doppler residuals with black dots and a moving average (computed on a sliding window of 5 data points) with a solid red line. Note that a count time of 1 s for the observables was chosen for PJ53 occultation, whereas a count time of 0.1 s was selected for PJ63. As a measure of the noise observed during these occultations, we report in the lower panels the quantity δf, defined as the difference between the collected Doppler data points and a moving average. To quantify the impact of this noise, we conducted Monte Carlo analyses. Specifically, Gaussian random noise time series, with a standard deviation corresponding to the observed noise levels, were added to the original Doppler frequency residuals (Schinder et al., 2011b). This method enabled the calculation of multiple pressure-temperature profiles, which were subsequently used to estimate the associated error bars.

As previously explained, in the process of retrieving the vertical atmospheric profiles, the knowledge of the position of all elements involved in the radio occultation experiment is required. For this purpose, we utilize the planetary ephemerides and the spacecraft's trajectory as reconstructed by Juno's Navigation Team. This trajectory

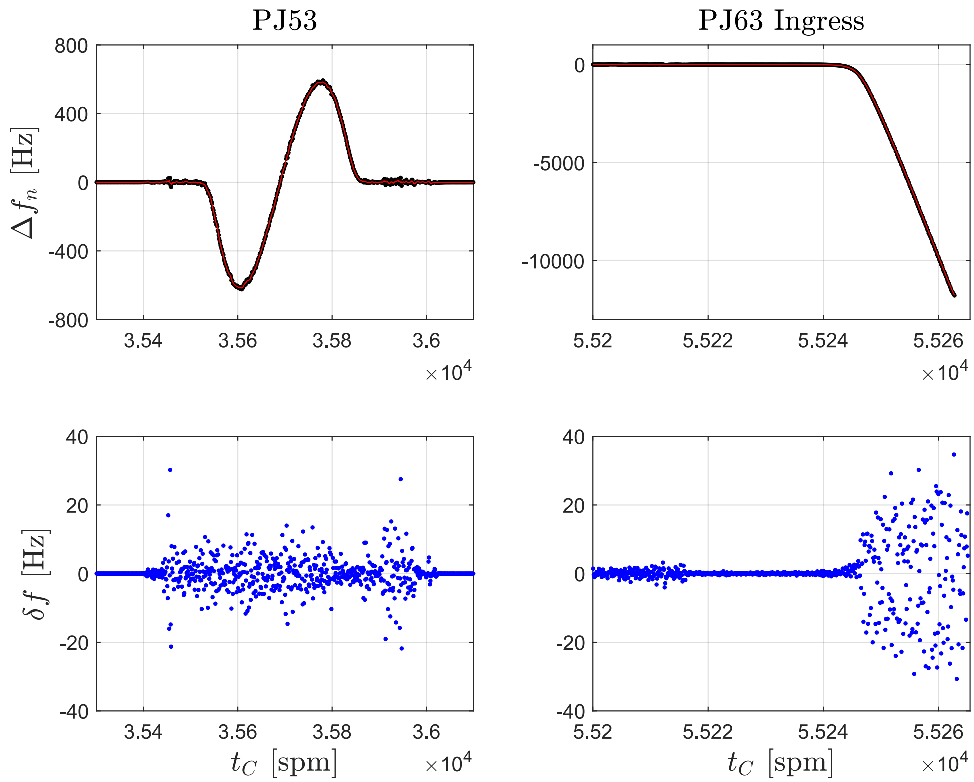

Figure 2. Doppler frequency residuals (black points) for the occultations occurred during PJ53 (left) and PJ63 (right) are depicted in the upper panels, along with a moving average of the data (red line). The lower panels report the difference between the Doppler data points and the moving average.

carries an inherent uncertainty, which in turn affects the measurements of atmospheric properties. To assess the impact of this uncertainty, several Juno trajectories were generated, all compatible with the reconstructed trajectory produced by the Juno Navigation Team. These were then used as input for the inversion code to derive multiple pressure-temperature profiles, used to evaluate the uncertainties (Parisi et al., 2023).

4. Jupiter Atmospheric Profiles

This section presents the pressure-temperature profiles of Jupiter's atmosphere along with their uncertainties. For the sake of conciseness, we will display only a subset of the profiles for selected occultations. Additional profiles are reported in a companion paper (Smirnova et al., 2025).

4.1. PJ53

On 31 July 2023, during PJ53, Juno executed the first atmospheric occultation of Jupiter. NASA's DSN-53 antenna supported this pass, transmitting the uplink signal at X-band, and recording downlink signals at X- and Ka-bands. Due to the grazing geometry of this occultation, the X-band signal was continuously observed, but Ka-band was lost.

The Doppler residual frequency for this occultation is shown in Figure 2 considering a count time of 1 sec. This first occultation was particularly noisy; this caused the ray-tracing-based method to encounter convergence problems. For this reason, we resorted to frequency smoothing, in particular a Savitsky-Golay filter (Gorry, 1990). This approach was already used in the past literature for occultation data analyses (Schinder et al., 2020), but we used this approach for this case only since this technique may smooth away actual atmospheric structures. As shown in the upper panels of Figure 3, in the upper atmosphere the total uncertainty (shown with a blue area) can reach values higher than 20 K, and is dominated by the noise in the observables. At a pressure of 100 mbar, we measured a temperature of 119.7 ± 2.7 K in ingress and 121.2 ± 2.5 K in egress. This pressure

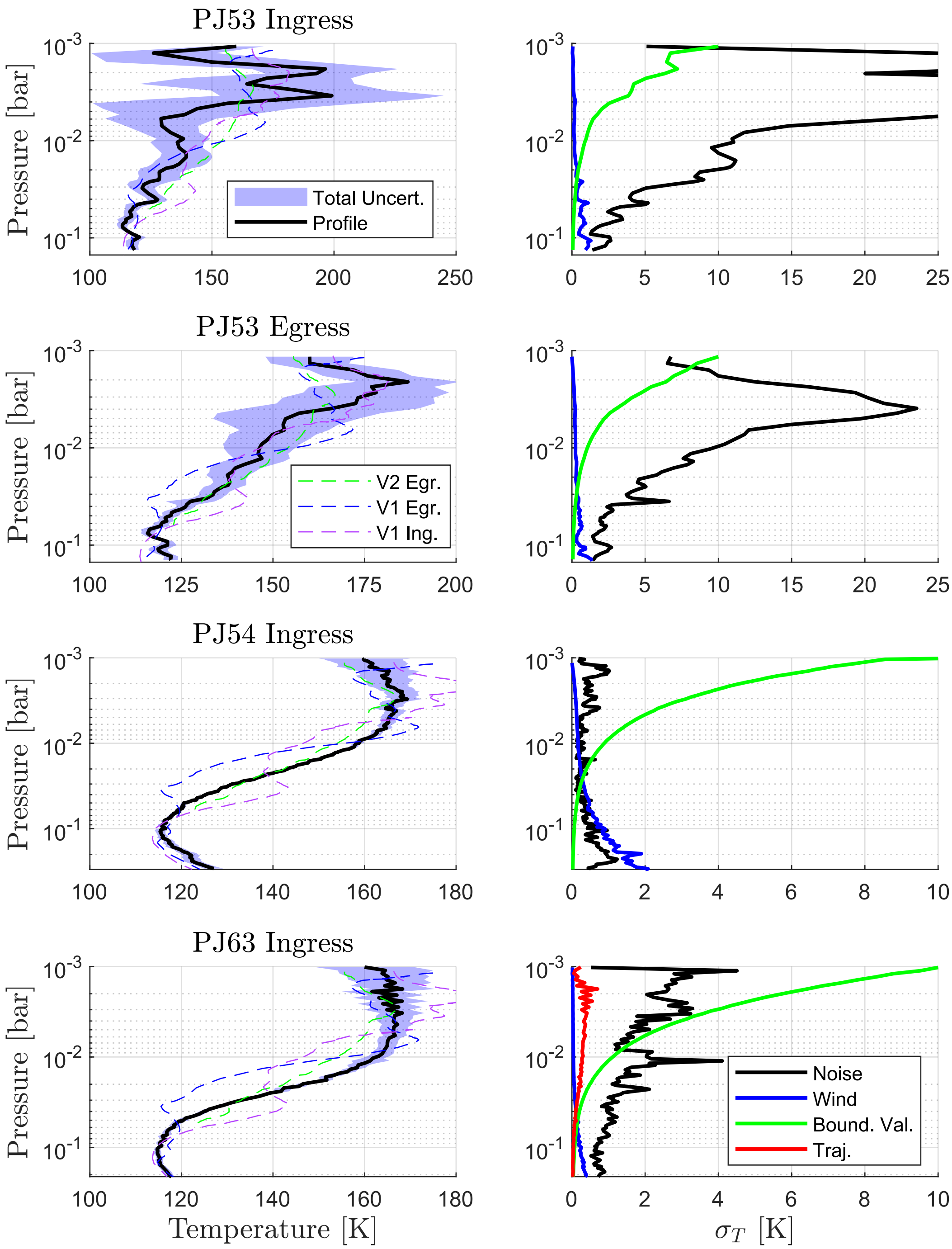

Figure 3. Pressure-temperature profiles for the occultations occurred during PJ53, 54, and 63. The panels on the right show the contribution of different factors to the total uncertainties (the blue area in the left panels). Atmospheric profiles from Voyager occultations are depicted with dashed lines (Gupta et al., 2022).

was measured at a radius of 70188 km at a latitude of 30.85 deg during ingress, and 70803 km at a latitude of 22 deg during egress.

4.2. PJ54

Juno executed the PJ54 pass on 7 September 2023, which included the second occultation of Jupiter. Goldstone's DSS-25 antenna supported this experiment. This PJ was conducted using a slightly modified Earth-point attitude

$<0.1-$degree off, in order to sound a little deeper into the atmosphere during the ingress phase. Furthermore, this was the only occultation up to now to use the onboard Ka-band Translator (Asmar et al., 2017); therefore, the mode X/X + Ka/Ka described above was used.

The profile for the ingress phase of this occultation is shown in the third row of Figure 3, along with the uncertainties due to the different factors (right panel). The total uncertainty is dominated by the unknown boundary value at 1 mbar level, whereas the main factor at lower altitudes is the noise in the observables and wind uncertainty. Indeed, at 100 mbar, we measure a temperature of 116.2 ± 1 K at a radial distance of 69847 km from Jupiter barycenter and a latitude of 35.25 deg.

4.3. PJ63

Juno executed the PJ63 pass above Jupiter on the 16 July 2024. This was the first auroral-zone occultation. The occultation data were taken at Goldstone's DSS-25 antenna. The radio link was configured for mode X/X + X/Ka. The Doppler residual frequency for this experiment in depicted in Figure 2. The resulting pressure-temperature profile is shown in the lower left panel of Figure 3. The right lower panel shows that the measurement error associated to the Juno's trajectory and wind measurements uncertainties is negligible with respect to the effect due to the noise in the observable or due to the unknown boundary value of temperature at 1 mbar. For this occultation, a temperature of 115 ± 0.7 K was measured at 100 mbar level, when the radius is 67769 km and the latitude is 62.68 deg.

5. Discussion

The new measurements of pressure and temperature obtained from the analyses of Juno's radio occultation experiments have provided valuable data to study Jupiter's atmospheric dynamics; all details can be found in a companion paper by Smirnova et al. (2025). These new measurements are consistent with previous findings from Voyager occultation experiments (Gupta et al., 2022; Lindal et al., 1981) as depicted in Figure 3. More vertical profiles obtained from the other Juno's occultation experiments can be found in Smirnova et al. (2025). Additionally, as a result of our analysis we have also assessed the latitudes and radii at the 100 mbar pressure level, which may be used in the determination of an updated shape model of Jupiter (Galanti et al., 2023; Lindal et al., 1985).

It should be noted that the original Juno mission did not include any radio occultation experiments. In fact, the spacecraft lacks an Ultra-Stable Oscillator (USO), which would have enabled one-way radio occultations. For this reason, Juno's occultations are two-way experiments. This generally complicates data analysis since a specialized method for two-way occultations is required, as the one described in this paper, which also requires high computational cost. Additionally, in a two-way experiment, a certain amount of time is required to acquire the signal during an egress occultation. This lead to loss of data immediately after the occultation. In this case, a snap-lock technique must be used to reacquire the signal during the egress phase, preventing loss of data (Buccino et al., 2022). However, two-way occultations can offer advantages in terms of oscillator's output frequency stability. Indeed, typical space-based USO are less stable if compared to ground-based oscillators (Withers, 2010). The use of an USO may then lead to higher uncertainties in the retrieved vertical profiles. Moreover, Juno maintains a fixed orientation during occultations, unlike missions such as Cassini, where the spacecraft's attitude was adjusted to ensure the high-gain antenna remained aligned with the Earth's virtual image as seen through Saturn's atmosphere. For Juno, this fixed orientation means that, due to the limited beamwidth, the signal is lost at relatively high altitudes, preventing it from probing the atmosphere down to higher pressure levels (as done by Cassini or Voyager missions).

With several occultations already conducted, and more expected in future perijoves, Juno's findings will ultimately enable the construction of a global map of Jupiter's atmospheric properties across various latitudes and different conditions, deepening our understanding of the planet's atmospheric dynamics.

Conflict of Interest

The authors declare no conflicts of interest relevant to this study.

Data Availability Statement

The radio occultation data collected by Juno and utilized in this manuscript can be accessed publicly via NASA's Planetary Data System (Buccino, 2016).

Acknowledgments

AC, LGC, MZ, EG, AT, and PT are grateful to the Italian Space Agency (ASI) for financial support through Agreement No. 2023-6-HH.0 in the context of ESA's JUICE mission, and Agreement No. 2022-16-HH.1-2024, for ESA's BepiColombo and NASA's Juno radio science experiments. The work of DB, MP, RP, and SL was carried out at the Jet Propulsion Laboratory, California Institute of Technology, under a contract with the National Aeronautics and Space Administration. Government sponsorship acknowledged. Open access publishing facilitated by Universita degli Studi di Bologna, as part of the Wiley - CRUI-CARE agreement.

References

Acton, C. H. (1996). Ancillary data services of NASA’s navigation and Ancillary information facility. *Planetary and Space Science*, *44*(1), 65–70. https://doi.org/10.1016/0032-0633(95)00107-7

Asmar, S. W., Bolton, S. J., Buccino, D. R., Cornish, T. P., Folkner, W. M., Formaro, R., et al. (2017). The Juno gravity science instrument. *Space Science Reviews*, *213*(1–4), 205–218. https://doi.org/10.1007/s11214-017-0428-7

Bolton, S. J., Lunine, J., Stevenson, D., Connerney, J. E. P., Levin, S., Owen, T. C., et al. (2017). The Juno Mission. *Space Science Reviews*, *213*(1–4), 5–37. https://doi.org/10.1007/s11214-017-0429-6

Bourgoin, A., Zannoni, M., & Tortora, P. (2019). Analytical ray-tracing in planetary atmospheres. *Astronomy and Astrophysics*, *624*, A41. https://doi.org/10.1051/0004-6361/201834962

Buccino, D. (2016). Juno Jupiter gravity science raw data set v1.0 [dataset]. *NASA Planetary Data System (PDS)*. Retrieved from https://atmos.nmsu.edu/PDS/data/jnogrv_1001/

Buccino, D., Parisi, M., Gramigna, E., Gomez-Casajus, L., Tortora, P., Zannoni, M., et al. (2022). Ganymede’s ionosphere observed by a dual-frequency radio occultation with juno. *Geophysical Research Letters*, *49*(23), e2022GL098420. https://doi.org/10.1029/2022GL098420

Buccino, D., Parisi, M., Kahan, D., Wilson, H., Yang, O., Barbinis, E., et al. (2023). Planning and execution of Juno radio occultation experiments at Jupiter. In *2023 IEEE aerospace conference*. https://doi.org/10.1109/AERO55745.2023.10115541

Caruso, A., Bourgoin, A., Togni, A., Zannoni, M., & Tortora, P. (2023). Radio occultation data analysis with analytical ray-tracing. *Radio Science*, *58*(9), 1–22. https://doi.org/10.1029/2023RS007740

Chang, C. (2015). Telecommunications link design handbook. *DSN Document*, *373*, 810–005. https://deepspace.jpl.nasa.gov/dsndocs/810-005/Binder/810-005_Binder_Change44.pdf

Dalba, P. A., & Withers, P. (2019). Cassini radio occultation observations of Titan’s ionosphere: The complete set of electron density profiles. *Journal of Geophysical Research*, *124*(1), 643–660. https://doi.org/10.1029/2018JA025693

Durante, D., Parisi, M., Serra, D., Zannoni, M., Notaro, V., Racioppa, P., et al. (2020). Jupiter’s gravity field halfway through the Juno mission. *Geophysical Reseach Letters*, *47*(22), e2019GL086572. https://doi.org/10.1029/2019GL086572

Fjeldbo, G., & Eshleman, V. R. (1968). The atmosphere of Mars analyzed by integral inversion of the Mariner IV occultation data. *Planetary and Space Science*, *16*(8), 1035–1059. https://doi.org/10.1016/0032-0633(68)90020-2

Galanti, E., Kaspi, Y., & Guillot, T. (2023). The shape of Jupiter and Saturn based on atmospheric dynamics, radio occultations and gravity measurements. *Geophysical Research Letters*, *50*(6), e2022GL102321. https://doi.org/10.1029/2022GL102321

Gorry, P. A. (1990). General least-squares smoothing and differentiation by the convolution (Savitzky-Golay) method. *Analytical Chemistry*, *62*(6), 570–573. https://doi.org/10.1021/ac00205a007

Gramigna, E., Parisi, M., Buccino, D., Casajus, L. G., Zannoni, M., Bourgoin, A., et al. (2023). Analysis of NASA’s DSN Venus Express radio occultation data for year 2014. *Advances in Space Research*, *71*(1), 1198–1215. https://doi.org/10.1016/j.asr.2022.10.070

Gupta, P., Atreya, S. K., Steffes, P. G., Fletcher, L. N., Guillot, T., Allison, M. D., et al. (2022). Jupiter temperature structure: A reassessment of the voyager radio occultation measurements. *The Planetary Science Journal*, *3*(159), 1–11. https://doi.org/10.3847/PSJ/ac6956

Hinson, D. P., Flasar, F. M., Kliore, A. J., Schinder, P. J., Twicken, J. D., & Herrera, R. G. (1997). Jupiter’s ionosphere: Results from the first Galileo radio occultation experiment. *Geophysical Research Letters*, *24*(17), 2107–2110. https://doi.org/10.1029/97GL01608

Hinson, D. P., Linscott, I. R., Young, L. A., Tyler, G., Stern, S., Beyer, R., et al. (2017). Radio occultation measurements of Pluto’s neutral atmosphere with New Horizons. *Icarus*, *290*, 96–111. https://doi.org/10.1016/j.icarus.2017.02.031

Jenkins, J. M., Steffes, P. G., Hinson, D. P., Twicken, J. D., & Tyler, G. (1994). Radio occultation studies of the Venus atmosphere with the Magellan spacecraft: 2. Results from the October 1991 experiments. *Icarus*, *110*(1), 79–94. https://doi.org/10.1006/icar.1994.1108

Kliore, A., Cain, D. L., Levy, G. S., Eshleman, V. R., Fjeldbo, G., & Drake, F. D. (1965). Occultation experiment: Results of the first direct measurement of mars’s atmosphere and ionosphere. *Science*, *149*(3689), 1243–1248. https://doi.org/10.1126/science.149.3689.1243

Limaye, S. S. (1986). Jupiter: New estimates of the mean zonal flow at the cloud level. *Icarus*, *65*(2–3), 335–352. https://doi.org/10.1016/0019-1035(86)90142-9

Lindal, G. F., Sweetnam, D. N., & Eshleman, V. R. (1985). The atmosphere of Saturn: An analysis of the Voyager radio occultation measurements. *The Astronomical Journal*, *90*(6), 1136–1146. https://doi.org/10.1086/113820

Lindal, G. F., Wood, G. E., Levy, J. D., Anderson, J. D., Sweetnam, D. N., Hotz, H. B., et al. (1981). The atmosphere of Jupiter: An analysis of the Voyager radio occultation measurements. *Journal of Geophysical Research*, *86*(A10), 8721–8727. https://doi.org/10.1029/JA086iA10p08721

Mariotti, G., & Tortora, P. (2013). Experimental validation of a dual uplink multifrequency dispersive noise calibration scheme for Deep Space tracking. *Radio Science*, *48*(2), 111–117. https://doi.org/10.1002/rds.20024

Moirano, A., Gomez Casajus, L., Zannoni, M., Durante, D., & Tortora, P. (2021). Morphology of the Io plasma torus from Juno radio occultations. *Journal of Geophysical Research: Space Physics*, *126*(10), e2021JA029190. https://doi.org/10.1029/2021JA029190

Parisi, M., Caruso, A., Buccino, D., Gramigna, E., Withers, P., Gomez-Casajus, L., et al. (2023). Radio occultation measurements of Europa’s ionosphere from Juno’s close flyby. *Geophysical Reseach Letters*, *50*(22), e2023GL106637. https://doi.org/10.1029/2023GL106637

Pätzold, M., Häusler, B., Bird, M. K., Tellmann, S., Mattei, R., Asmar, S. W., et al. (2007). The structure of Venus’ middle atmosphere and ionosphere. *Nature*, *450*(7170), 657–660. https://doi.org/10.1038/nature06239

Phipps, P. H., Withers, P., Buccino, D. R., Yang, Y., & Parisi, M. (2021). Two years of observations of the Io plasma torus by Juno radio occultations: Results from perijoves 1 to 15. *Journal of Geophysical Research: Space Physics*, *126*(3), e2020JA028710. https://doi.org/10.1029/2020JA028710

Poisson, E., & Will, C. M. (2014). *Gravity*. Cambridge University Press. chap. 2. https://doi.org/10.1017/CBO9781139507486

Rife, D., & Boorstyn, R. (1974). Single tone parameter estimation from discrete-time observations. *IEEE Transactions on Information Theory*, *20*(5), 591–598. https://doi.org/10.1109/TIT.1974.1055282

Schinder, P. J., Flasar, F. M., Marouf, E. A., French, R. G., Anabtawi, A., Barbinis, E., et al. (2020). The structure of Titan’s atmosphere from Cassini radio occultations: One- and two-way occultations. *Icarus*, *345*, 113720. https://doi.org/10.1016/j.icarus.2020.113720

Schinder, P. J., Flasar, F. M., Marouf, E. A., French, R. G., Anabtawi, A., Barbinis, E., et al. (2015). A numerical technique for two-way radio occultations by oblate axisymmetric atmospheres with zonal winds. *Radio Science*, *50*(7), 712–727. https://doi.org/10.1002/2015RS005690

10.1029/2024GL113231

Schinder, P. J., Flasar, F. M., Marouf, E. A., French, R. G., McGhee, C. A., Kliore, A. J., et al. (2011a). Saturn's equatorial oscillation: Evidence of descending thermal structure from Cassini radio occultations. *Geophysical Research Letters*, *38*(8), L08205. https://doi.org/10.1029/2011GL047191

Schinder, P. J., Flasar, F. M., Marouf, E. A., French, R. G., McGhee, C. A., Kliore, A. J., et al. (2011b). The structure of Titan's atmosphere from Cassini radio occultations. *Icarus*, *215*(2), 460–474. https://doi.org/10.1016/j.icarus.2011.07.030

Simon-Miller, A. A., Conrath, B. J., Gierasch, P. J., Orton, G., Achterberg, R., Flasar, F., et al. (2006). Jupiter atmospheric temperatures: From Voyager IRIS to Cassini CIRS. *Icarus*, *180*(1), 98–112. https://doi.org/10.1016/j.icarus.2005.07.019

Smirnova, M., Galanti, E., Caruso, A., Fletcher, L. N., Buccino, D., Gomez Casajus, L., et al. (2025). Probing Jupiter's atmosphere through Juno radio occultations: Analysis of the atmospheric thermal structure. *Geophysical Reseach Letters*, *52*, e2025GL116804. https://doi.org/10.1029/2025GL116804

Tollefson, J., Wong, M. H., de Pater, I., Simon, A. A., Orton, G. S., Rogers, J. H., et al. (2017). Changes in jupiter's zonal wind profile preceding and during the juno mission. *Icarus*, *296*, 163–178. https://doi.org/10.1016/j.icarus.2017.06.007

Withers, P. (2010). Prediction of uncertainties in atmospheric properties measured by radio occultation experiments. *Advances in Space Research*, *46*(1), 58–73. https://doi.org/10.1016/j.asr.2010.03.004

Withers, P., & Moore, L. (2020). How to process radio occultation data: 2. from time series of two-way, single-frequency frequency residuals to vertical profiles of ionospheric properties. *Radio Science*, *55*(8), e2019RS007046. https://doi.org/10.1029/2019RS007046

Wong, M. H., Simon, A. A., Tollefson, J. W., de Pater, I., Barnett, M. N., Hsu, A. I., et al. (2020). High-resolution uv/optical/ir imaging of jupiter in 2016–2019. *The Astrophysical Journal - Supplement Series*, *247*(2), 1–25. https://doi.org/10.3847/1538-4365/ab775f